Robotica: (2020) volume 38, pp. 375–395. © Cambridge University Press 2019
doi:10.1017/S0263574719000687

Oscillation Reduction and Frequency Analysis of Under-Constrained Cable-Driven Parallel Robot with Three Cables

Sung Wook Hwang, Jeong-Hyeon Bak, Jonghyun Yoon and Jong Hyeon Park*

Department of Mechanical Engineering, Hanyang University, Seoul, Korea.
E-mails: gagys@naver.com, superrogin@gmail.com, potermk2@nate.com

(Accepted April 10, 2019. First published online: June 7, 2019)

SUMMARY
Cable-driven parallel robots (CDPRs) possess a lot of advantages over conventional parallel manipulators and link-based robot manipulators in terms of acceleration due to their low inertia. This paper deals with under-constrained CDPRs, which manipulate the end-effector to carrying the payload by using a number of cables less than six, often used preferably owing to their simple structures. Since a smaller number of cables than six are used, the end-effector of CDPR has uncontrollable degrees of freedom and that causes swaying motion and oscillations. In this paper, a scheme to curb on the unwanted oscillation of the end-effector of the CDPR with three cables is proposed based on multi-mode input shaping. The precise dynamic model of the under-constrained CDPR is obtained to find natural frequencies, which depends on the position of the end-effector. The advantage of the proposed method is that it is practicable to generate the trajectories for vibration suppression based on multi-mode input-shaping scheme in spite of the complexity in the dynamics and the difficulty in computing the natural frequencies of the CDPR, which are required in any input-shaping scheme. To prove the effectiveness of the proposed method, computer simulations and experiments were carried out by using 3-D motion for CDPR with three cables.

KEYWORDS: Under-constrained cable-driven parallel robot; Input shaping; Vibration; Natural frequency; Trajectory generation.

1. Introduction

Cable-driven parallel robots (CDPRs) employ several cables instead of rigid links to manipulate the pose of their end-effector. CDPRs have many advantages in comparison with conventional link-based parallel manipulators and serial-linked robot manipulators. Since CDPRs use low-inertia cables in place of rigid links, the total mass of moving parts is small and it can be possible for the end-effector to move fast or to carry a heavy load. Thus, CDPRs can exhibit the high performances in terms of speed, load manipulation, energy efficiency, so on. They can have broad workspace and have comparatively simple structure, making it easy to assemble and disassemble a CDPR system. These advantages enable them to be used more frequently in variety of application fields.[1–3]

CDPRs have some drawbacks, particularly caused by flexibility of the cables, such as oscillations of their end-effector and cable sagging due to cable weights. Also, one of the important characteristics of CDPRs is that the force that they can generate at their end-effector is the sum of *pulling*

* Corresponding author. E-mail: jongpark@hanyang.ac.kr

https://doi.org/10.1017/S0263574719000687 Published online by Cambridge University Press

forces by the cables since cables cannot exert a *pushing* force. As a result, a typical CDPR has more cables than the degrees of freedom (DOFs) of the end-effector in order to be able to exert any force and torque at the end-effector,[4–8] which are called over-constrained CDPRs or fully-constrained CDPRs.

Unlike over-constrained CDPRs, under-constrained CDPRs use fewer cables than the DOFs of the end-effector. So, the end-effector has uncontrollable DOFs in motion and it may not be possible to achieve any postures of the end-effector. And the vertical motion of the end-effector is controlled by the interaction between the vertical components of the pulling forces by the cables and the weight of the end-effector. Since under-constrained CDPRs use fewer number of cables compared with over-contrained CDPRs, their structure is simpler; therefore, they are less expensive and have a larger workspace based on perspective of collisions problems between the cables and the objects. Under-constrained CDPRs can be applied to many application fields such as measurement, rescue, service and construction yards.[9–12]

However, in under-constrained CDPR systems, the controllable workspace to satisfy desired pose of the end-effector may not exist and unwanted sway or oscillations of the end-effector may occur. Many researchers have been studying under-constrained CDPR systems to overcome their weakness. Planning the trajectory and finding the equilibrium point are a challenging problem of under-constrained CDPRs. Solving the forward and inverse kinematics under the kinematic constraints and the static balance of forces is a problem to be resolved.[13] One research group proposed a method to solve the forward and inverse kinematics of an under-constrained CDPR, and stability analysis of static equilibrium is assessed based on the geometrico-static model.[14–23] Oscillation damping of nonlinear system based on the phase trajectory length concept and anti-oscillation control were proposed for the under-constrained CDPR.[24]

Other research groups studied on planning trajectories for under-constrained CDPRs. A method to generate the trajectory on the basis of the inverse dynamic analysis was proposed in[25] and an antisway control method was proposed to suppress the oscillations of the end-effector in ref. [26]. And, trajectory tracking control of the end-effector was achieved by applying flatness-based control.[27] However, above-mentioned methods can be only applied to a special type, or crane-type manipulators,[28] which adjusts the cable length by using a winch installed at trolley. In refs. [29–31], a dynamic trajectory planning method was proposed based on a set of algebraic inequalities obtained from constraints on the cable tensions. It can be used to plan trajectories that extend beyond the static workspace of the under-constrained CDPR system. Another group proposed a geometrical approach to plan trajectories that also extend beyond static equilibrium workspace of the mechanism.[32] Despite of the fact these trajectory generation methods are useful to expend the workspace, they are too special and it is difficult for their methods to expanded to more general cases since they can generate the periodical trajectories. An anti-sway trajectory generation method was proposed by using input-shaping algorithm[33] and a neural network-based input-shaping method was proposed for an overhead crane.[34] A rest-to-rest trajectory planning method based on the solution of a boundary value problem was proposed[35], but the method only considers the 2-D planer case of the under-constrained CDPR. Although many trajectory planning methods have been proposed, trajectory generation to suppress unwanted sway and oscillations of the 3-D under-constrained CDPRs is still a challenge because of the complexity caused from the characteristic of 3-D under-constrained CDPR mechanism. To resolve these problems, our research group proposed the trajectory generation method based on input shaping for 3-D under-constrained CDPRs.[36] However, a single-mode input-shaping algorithm was applied by using an approximate natural frequency obtained from a simplified under-constrained CDPR model which is equal to an under-constrained CDPR with two cables in plane. Thus, this method involves the inaccuracy of the system model and can only be applied to the under-constrained CDPR system which has four cables and square shape workspace.

In this paper, a trajectory generation method for under-constrained CDPRs with *three* cables is proposed based on multi-mode input shaping to suppress unwanted oscillations of end-effector moving in 3-D space. The end-effector is suspended by three cables, and the orientation of the end-effector in equilibrium depends on the position of the end-effector. To solve inverse kinematics, the orientation with respect to the position of the end-effector is numerically analyzed by using the static equations and constraints. Natural frequencies of the CDPR required for the input-shaping method are analytically computed based on the Lagrange's equation of motion (EOM) and the linearization of the dynamics based on the perturbation method. The multi-mode input shaping is used to generate the

https://doi.org/10.1017/S0263574719000687 Published online by Cambridge University Press

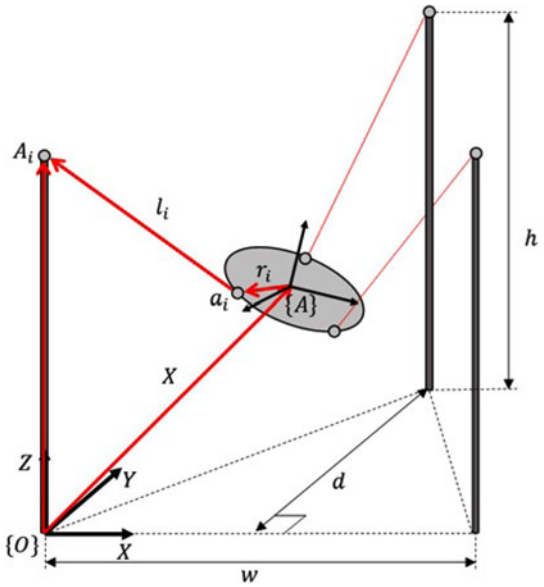


Fig. 1. Under-constrained CDPR model with three cables.

trajectory to suppress the oscillations by using the natural frequencies. Simulations and experiments of 3-D under-constrained CDPR motions were performed and their results showed that the proposed method is effective in significantly reducing the transient and residual oscillations of the end-effector.

This paper is organized as follows. Section 2 describes the kinematics and dynamics of the the CDPR with three cables, which is used in this work. The natural frequency analysis of the CDPR is done and the multi-mode input shaping based on the frequency found is applied in order to generate a vibration suppression trajectory in Section 3. Section 4 shows the effectiveness of the proposed method in computer simulations and experiments. Finally, a few conclusions are drawn in Section 5.

2. Kinematics and dynamics

2.1. CDPR model with three cables

An under-constrained CDPR with three cables, shown in Fig. 1, will be used in this study. It is assumed that the end-effector is a thin uniform disc and the three cables are assumed to be inextensible and massless. The length of each cable can be changed by its servo system with a pulley and a winch. The global coordinate frame $\{O\}$ is attached to the ground at one of the vertical posts, and a moving coordinate frame $\{A\}$ is attached at the COM of the end-effector, whose position is represented by

$$\mathbf{x} = [x \;\; y \;\; z]^T \in \mathbb{R}^3. \tag{1}$$

Cable i $(i = 1, 2, 3)$ that links Point a_i on the end-effector and its associated pulley position, Point A_i, can be represented by a vector

$$\boldsymbol{\ell}_i \triangleq \mathbf{A}_i - \mathbf{a}_i. \tag{2}$$

And $\mathbf{r}_i \in \mathbb{R}^3$ denotes the position vector from the COM of the end-effector to Point a_i and it can be written as

$$\mathbf{r}_i = \mathbf{R}_A^O \, {}^A\mathbf{r}_i,$$

where ${}^A\mathbf{r}_i$ is the vector r_i expressed by Coordinate Frame $\{A\}$ and $\mathbf{R}_A^O$ denotes the rotation matrix between the coordinate frames $\{O\}$ and $\{A\}$. Note that ${}^A\mathbf{r}_i$ is a constant vector.

Since the end-effector is constrained by three cables in 3-D space, the under-constrained CDPR system has three uncontrollable DOFs and it can lead to unwanted sway or oscillations of the end-effector.

https://doi.org/10.1017/S0263574719000687 Published online by Cambridge University Press

2.2. Dynamics and kinematic constraints

Motions of the end-effector have controlled by the servo system and it is constrained by kinematic constraints expressed by Eq. (3):

$$\mathbf{x} = \mathbf{A}_i - \mathbf{R}_A^O \, {}^A\mathbf{r}_i - \boldsymbol{\ell}_i, \quad (i = 1, 2, 3). \tag{3}$$

The number of these kinematic constraints is equal to the number of cables. Rotation matrix, $\mathbf{R}_A^O$, denotes the orientation of the end-effector with respect to the global coordinate frame $\{O\}$. With the use of by Z-Y-X Euler angle based on Tait-Bryan angles, the rotation matrix can be expressed by

$$\mathbf{R}_A^O \triangleq \begin{bmatrix} c_\psi c_\theta & c_\psi s_\theta s_\phi - c_\phi s_\psi & c_\phi c_\psi s_\theta + s_\phi s_\psi \\ c_\theta s_\psi & c_\phi c_\psi + s_\theta s_\phi s_\psi & -s_\phi c_\psi + c_\phi s_\theta s_\psi \\ -s_\theta & c_\theta s_\phi & c_\theta c_\phi \end{bmatrix}, \tag{4}$$

where ψ, θ and ϕ denote yaw, pitch and roll angles, respectively. For notational brevity, 's' and 'c' denote sine and cosine functions, respectively.

To obtain the Lagrange's EOM, the position and orientation parameters of the end-effector are selected as generalized coordinates,

$$\boldsymbol{q} = [\mathbf{x}^T \ \boldsymbol{\eta}^T]^T, \tag{5}$$

where

$$\boldsymbol{\eta} \triangleq [\phi \ \theta \ \psi]^T. \tag{6}$$

And angular velocity, $\boldsymbol{\omega}$, expressed with respect to Coordinate Frame $\{A\}$ is

$$\boldsymbol{\omega} = \mathbf{W}(\boldsymbol{\eta})\dot{\boldsymbol{\eta}}, \tag{7}$$

where

$$\mathbf{W}(\boldsymbol{\eta}) = \begin{bmatrix} 1 & 0 & -s_\theta \\ 0 & c_\phi & s_\phi c_\theta \\ 0 & -s_\phi & c_\phi c_\theta \end{bmatrix}. \tag{8}$$

Thus, the kinetic energy of the end-effector is the sum of the translational kinetic energy evaluated in the global coordinate frame $\{O\}$ and the rotational kinetic energy evaluated in the moving coordinate frame $\{A\}$ and it can be expressed by

$$K = \frac{1}{2} m \dot{\mathbf{x}}^T \dot{\mathbf{x}} + \frac{1}{2} \dot{\boldsymbol{\eta}}^T \mathbf{W}^T(\boldsymbol{\eta}) \mathbf{I}_G \mathbf{W}(\boldsymbol{\eta}) \dot{\boldsymbol{\eta}}, \tag{9}$$

where m and $\mathbf{I}_G$ denote the mass and the moment of inertia of the end-effector, respectively.

The potential energy of the end-effector that depends on the gravitational force is

$$V = mg \, \mathbf{e}_z^T \mathbf{x}, \tag{10}$$

with $\mathbf{e}_z \triangleq [0 \ 0 \ 1]^T$.

The Lagrangian is defined as

$$\begin{aligned} \mathcal{L} &\triangleq K - V \\ &= \frac{1}{2} m \dot{\mathbf{x}}^T \dot{\mathbf{x}} + \frac{1}{2} \dot{\boldsymbol{\eta}}^T \mathbf{W}^T(\boldsymbol{\eta}) \mathbf{I}_G \mathbf{W}(\boldsymbol{\eta}) \dot{\boldsymbol{\eta}} - mg \, \mathbf{e}_z^T \mathbf{x}. \end{aligned} \tag{11}$$

The kinematic constraints in Eq. (3) can be written as

$$\phi_i(\boldsymbol{q}) = 0 \quad \text{for } i = 1, 2, 3, \tag{12}$$

where

$$\phi_i(\boldsymbol{q}) \triangleq \|\mathbf{x} + \mathbf{R}_A^O(\boldsymbol{\eta}) \, {}^A\mathbf{r}_i - \mathbf{A}_i\|^2 - \|\boldsymbol{\ell}_i\|^2. \tag{13}$$

https://doi.org/10.1017/S0263574719000687 Published online by Cambridge University Press

It is possible to define the extended Lagrangian to reflect the holonomic constraints, $\boldsymbol{\phi} = \mathbf{0}$, as

$$\mathcal{L}_e \triangleq \mathcal{L} + \sum_{i=1}^{3} \phi_i \lambda_i = \mathcal{L} + \boldsymbol{\phi}^T \boldsymbol{\lambda}, \tag{14}$$

where ϕ_i and λ_i, respectively, denote the i-th component of $\boldsymbol{\phi} \in \mathbb{R}^3$ and $\boldsymbol{\lambda} \in \mathbb{R}^3$. Note that the latter represents the constraint force, that is, the cable tensions.

Then, the Lagrange's EOM can be written as

$$\frac{d}{dt}\left(\frac{\partial \mathcal{L}_e}{\partial \dot{\boldsymbol{q}}}\right) - \frac{\partial \mathcal{L}_e}{\partial \boldsymbol{q}} = \mathbf{0} \tag{15a}$$

or

$$\frac{d}{dt}\left(\frac{\partial \mathcal{L}}{\partial \dot{\boldsymbol{q}}}\right) - \frac{\partial \mathcal{L}}{\partial \boldsymbol{q}} = \left(\frac{d\boldsymbol{\phi}}{d\boldsymbol{q}}\right)^T \boldsymbol{\lambda}. \tag{15b}$$

This equation combined with Eq. (12) describes the dynamics of the CDPR.

2.3. Static equilibrium of end-effector

Let's find the equilibrium points of the under-constrained CDPR system, satisfying $\ddot{\mathbf{q}} = \dot{\mathbf{q}} = \mathbf{0}$, where the natural frequency of the system will be found later. Since $\partial \mathcal{L}/\partial \dot{\mathbf{q}} = \mathbf{0}$ with $\ddot{\mathbf{q}} = \dot{\mathbf{q}} = \mathbf{0}$, and the Lagrangian in Eq. (11), Eq. (15b) becomes

$$\frac{\partial \mathcal{L}}{\partial \boldsymbol{q}} + \left(\frac{d\boldsymbol{\phi}}{d\boldsymbol{q}}\right)^T \boldsymbol{\lambda} = \mathbf{0}. \tag{16}$$

Note that there exist *nine* equations: *three* constraint equations of Eq. (12) and *six* equations of Eq. (16). Note also that there are *12* unknowns: $\mathbf{x}_0$, $\boldsymbol{\eta}_0$, $\boldsymbol{\lambda}_0$ and $\|\ell_i\|$ for $i = 1, 2, 3$. Here, the symbols with subsection '0' denote quantities at a static equilibrium. Therefore, if $\mathbf{x}_0$ is fixed, all the other unknowns including $\boldsymbol{\eta}$ can be determined. Note that among many solutions, only the one with $\lambda_{i,0} > 0$ for all $i = 1, 2, 3$, implying positive tensions at all the cables, is valid. After all, this means that there exists a mapping $\varphi : \mathbf{x}_0 \rightarrow \boldsymbol{\eta}_0$.

As an example, let's consider a 3-cable CDPR which will be used through out the work. In it, the three pulleys are elevated 2 m from the ground and their projected positions on the ground form an isosceles triangle with 2-m base and 2-m height. Figure 2 shows how the orientation angles change as the horizontal position of the end-effector changes at $z = 0.5$ m, 1 m or 1.5 m. The tilting angle of the end-effector with a horizontal plane increases rapidly as the end-effector approaches to the edges of its workspace. The range of the tilting in horizontal motions shrinks as z increases. Here, the end-effector is assumed to be a circular disk with radius of 0.115 m and the ends of the three cables on the end-effector form an equilateral triangle, similar to the pulleys. Notice that mapping φ depends on the size of the end-effector and the locations where the ends of the cables are connected to the end-effector.

3. Trajectory generation to suppress oscillations

3.1. Natural frequencies of CDPR

To generate the trajectory to suppress the unwanted vibrations of the CDPR by applying the input-shaping algorithm, the natural frequency of the CDPR should be found. If the end-effector is constrained by n (< 6) independent cables, motions of the CDPR have $(6 - n)$ DOFs. For a 3-cable CDPR, it has three DOFs and thus three modes.

By splitting the dynamics in Eq. (15) into two based on the states, $\mathbf{x}$ and $\boldsymbol{\eta}$, and then removing the Lagrange multiplier $\boldsymbol{\lambda}$,

$$\begin{aligned}\mathbf{0} &= \boldsymbol{\Phi}_x^{-T}\left[\frac{d}{dt}\left(\frac{\partial \mathcal{L}}{\partial \dot{\mathbf{x}}}\right) - \frac{\partial \mathcal{L}}{\partial \mathbf{x}}\right] - \boldsymbol{\Phi}_\eta^{-T}\left[\frac{d}{dt}\left(\frac{\partial \mathcal{L}}{\partial \dot{\boldsymbol{\eta}}}\right) - \frac{\partial \mathcal{L}}{\partial \boldsymbol{\eta}}\right] \\ &\triangleq \boldsymbol{\xi}(\boldsymbol{q}),\end{aligned} \tag{17}$$

https://doi.org/10.1017/S0263574719000687 Published online by Cambridge University Press

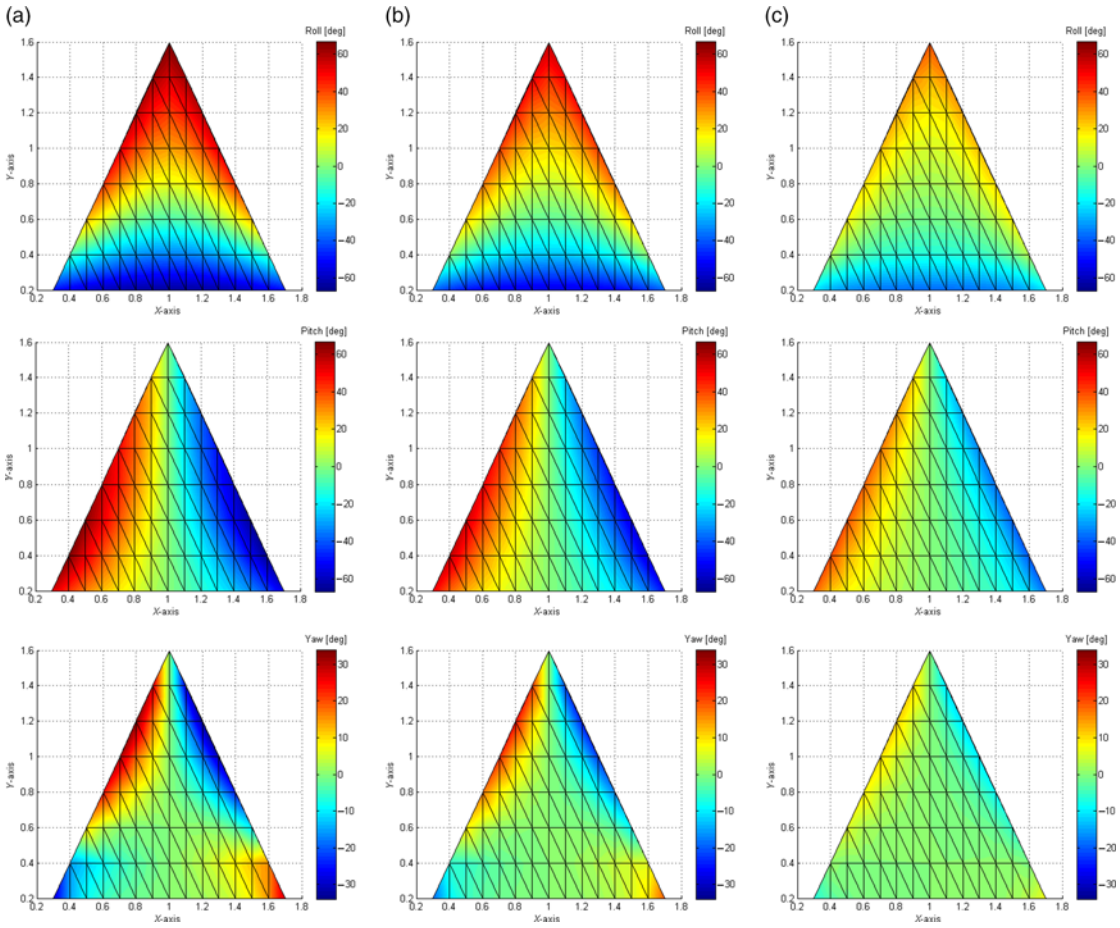


Fig. 2. Relation between the orientation and the position of the end-effector at static equilibrium states on a horizontal plane at (a) $z = 0.5$ m, (b) $z = 1$ m and (c) $z = 1.5$ m.

where

$$\mathbf{\Phi}_u(\mathbf{q}) \triangleq \frac{\partial \boldsymbol{\phi}}{\partial \mathbf{u}} \in \mathbb{R}^{3\times 3}.$$

By linearizing the nonlinear dynamics in Eq. (17) around an equilibrium point based on the perturbation method,[37] it is possible to find the CDPR's natural frequencies.

When the end-effector oscillates around the any equilibrium point, the position and the orientation of the end-effector can be expressed as

$$\mathbf{x}(t) = \mathbf{x}_0 + \delta\mathbf{x}(t), \tag{18}$$
$$\boldsymbol{\eta}(t) = \boldsymbol{\eta}_0 + \delta\boldsymbol{\eta}(t), \tag{19}$$

where $\delta\mathbf{x}(t)$ and $\delta\boldsymbol{\eta}(t)$ denote the perturbations around the equilibrium point with $\mathbf{x}_0$ and $\boldsymbol{\eta}_0$.

By neglecting the quadratic and higher-order terms of the perturbation variables, which is possible because the effect of that terms is very small on the system when the perturbation is bounded in small range, Eq. (17) can be simplified as

$$\mathbf{M}_x\delta\ddot{\mathbf{x}} + \mathbf{M}_\eta\delta\ddot{\boldsymbol{\eta}} + \mathbf{K}_x\delta\mathbf{x} + \mathbf{K}_\eta\delta\boldsymbol{\eta} = \mathbf{0}, \tag{20}$$

https://doi.org/10.1017/S0263574719000687 Published online by Cambridge University Press

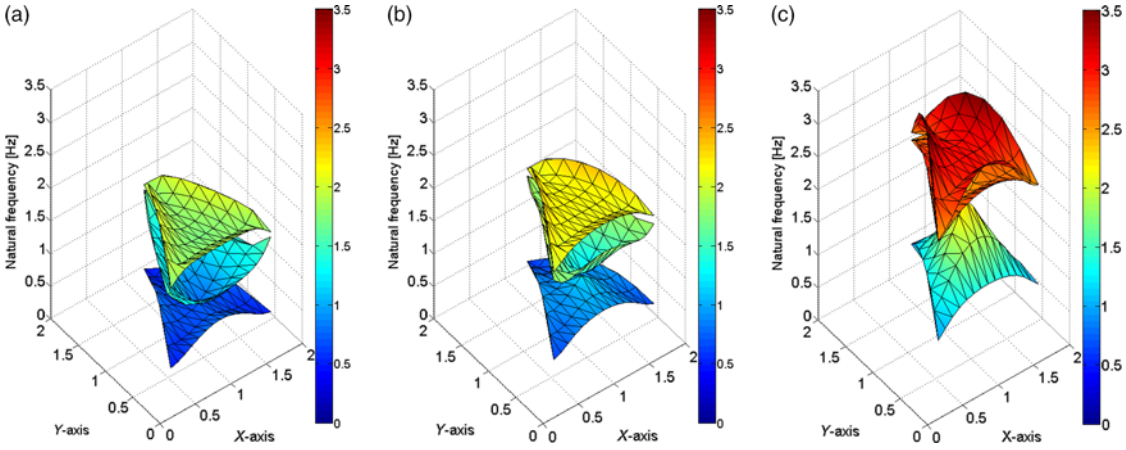


Fig. 3. Tendency of natural frequencies depending on the location of the end-effector at (a) $z = 0.5$ m, (b) $z = 1$ m and (c) $z = 1.5$ m.

where

$$\mathbf{M}_x = \left.\frac{\partial \boldsymbol{\xi}}{\partial \ddot{\mathbf{x}}}\right|_0, \quad \mathbf{M}_\eta = \left.\frac{\partial \boldsymbol{\xi}}{\partial \ddot{\boldsymbol{\eta}}}\right|_0,$$
$$\mathbf{K}_x = \left.\frac{\partial \boldsymbol{\xi}}{\partial \mathbf{x}}\right|_0, \quad \mathbf{K}_\eta = \left.\frac{\partial \boldsymbol{\xi}}{\partial \boldsymbol{\eta}}\right|_0.$$

To find the natural frequencies, Eq. (20) should be composed as the function of three perturbation variables. In this paper, three perturbation variables to fine the natural frequencies are selected as one perturbation vector which is $\delta\mathbf{x}$ or $\delta\eta$. The relationship of two perturbation vectors can be expressed from the linearized equation of kinematic constraints of Eq. (12) as follows:

$$\boldsymbol{\Phi}_{x,0}\,\delta\mathbf{x} + \boldsymbol{\Phi}_{\eta,0}\,\delta\boldsymbol{\eta} = \mathbf{0}, \tag{21}$$
$$\boldsymbol{\Phi}_{x,0}\,\delta\dot{\mathbf{x}} + \boldsymbol{\Phi}_{\eta,0}\,\delta\dot{\boldsymbol{\eta}} = \mathbf{0}, \tag{22}$$
$$\boldsymbol{\Phi}_{x,0}\,\delta\ddot{\mathbf{x}} + \boldsymbol{\Phi}_{\eta,0}\,\delta\ddot{\boldsymbol{\eta}} = \mathbf{0}, \tag{23}$$

with $\boldsymbol{\Phi}_{x,0} \triangleq \boldsymbol{\Phi}_x(\boldsymbol{q}_0) \in \mathbb{R}^{3\times 3}$ and $\boldsymbol{\Phi}_{\eta,0} \triangleq \boldsymbol{\Phi}_\eta(\boldsymbol{q}_0) \in \mathbb{R}^{3\times 3}$. For more details on them, refer to Appendix A.

By combining Eqs. (20), (21), (22) and (23), the linearized dynamic equation of the system can be expressed in terms of single perturbation variable, $\delta\boldsymbol{\eta}$:

$$\left(\mathbf{M}_\eta - \mathbf{M}_x\boldsymbol{\Phi}_{x,0}^{-1}\boldsymbol{\Phi}_{\eta,0}\right)\delta\ddot{\boldsymbol{\eta}} + \left(\mathbf{K}_\eta - \mathbf{K}_x\boldsymbol{\Phi}_{x,0}^{-1}\boldsymbol{\Phi}_{\eta,0}\right)\delta\boldsymbol{\eta} = \mathbf{0}. \tag{24a}$$

or

$$\delta\ddot{\boldsymbol{\eta}} + \boldsymbol{\Omega}^2\delta\boldsymbol{\eta} = \mathbf{0}, \tag{24b}$$

where

$$\boldsymbol{\Omega}^2 \triangleq \left(\mathbf{M}_\eta - \mathbf{M}_x\boldsymbol{\Phi}_{x,0}^{-1}\boldsymbol{\Phi}_{\eta,0}\right)^{-1}\left(\mathbf{K}_\eta - \mathbf{K}_x\boldsymbol{\Phi}_{x,0}^{-1}\boldsymbol{\Phi}_{\eta,0}\right). \tag{25}$$

Note that the eigenvalues of matrix $\boldsymbol{\Omega}^2$ are the natural frequencies of the system and that they depend on the equilibrium position and orientation of the end-effector, $\boldsymbol{q}_0$.

How the *three* natural frequencies change as the end-effector of the CDPR described in Section 2.3 moves horizontally at a different height is shown in Fig. 3. Two of the highest natural frequencies rapidly increase (the lowest frequency gradually decreases) as the end-effector moves horizontally toward the workspace boundary.

3.2. Designing of multi-mode input shaper

Input-shaping method can be used to reduce the vibration by modifying the original command input signal, and the modified command input signal is self-canceling.[38–40] The modified command input

https://doi.org/10.1017/S0263574719000687 Published online by Cambridge University Press

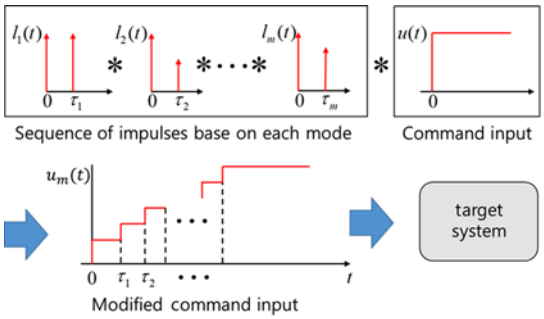


Fig. 4. Process of m-mode multi-mode input shaping.

signal with vibration canceling characteristic is formed through convolution with original command input and a sequence of impulses which can be formed based on the natural frequency of the system. The sequence of impulses can be expressed by

$$l(t) = \sum_{i=0}^{n} A_i \delta(t - \tau_i), \tag{26}$$

where n is the number of impulses required to reduce vibration and A_i is magnitude of each impulse at time τ_i. All of the A_i should be larger than 0 and its sum should be 1, that is, $\sum A_i = 1$.

In this work, multi-mode input-shaping algorithm based on Zero-Vibration (ZV) shaper is used to generate modified command input to suppress the unwanted oscillations caused by uncontrollable DOF of the under-constrained CDPR system. Figure 4 shows the process of m-mode input-shaping algorithm, where $u(t)$ means the original command input signal, $l(t)$ is a sequence of impulses with respect to each mode and $y(t)$ is the modified command input signal to suppress the oscillations. When the target system has m-mode, the number of the impulse to convolute with original command input is 2^m. The sequence of impulses based on each mode is generated:

$$l_a(t) = \sum_{i=0}^{1} A_i \delta(t - \tau_i), \quad (a = 1, \ldots, m), \tag{27}$$

where m is the number of modes and

$$\begin{bmatrix} A_i \\ \tau_i \end{bmatrix} = \begin{bmatrix} K_i/(1+K_i) & 1/(1+K_i) \\ 0 & \pi/\omega_{n,i} \end{bmatrix}, \quad (i = 0, 1). \tag{28}$$

Here, $K_i = \exp(-\zeta_i \pi / \sqrt{1-\zeta_i^2})$, which defines the magnitudes of the impulses, depends on the damping ratio ζ_i only. The time of an impulse, τ_i, can be obtained by using the natural frequency of the target system.

Next, in order to generate the modified command input signal, $y(t)$, the original command input signal, $u(t)$, which is the desired trajectory of the end-effector, is convoluted with these sequences of impulses:

$$u_m(t) = l_1(t) * l_2(t) * \cdots * l_m(t) * u(t). \tag{29}$$

The number of modes of the under-constrained CDPR is equal to the uncontrollable DOFs. And, since there is no damping in the system, that is, in Eq. (24b), the damping ratios are all zero and thus the magnitude of impulses, A_i, is 0.5.

4. Simulations and experiments

4.1. Simulations

In order to measure the performance and to prove the effectiveness of the proposed method, computer simulations were conducted with commercial software: Matlab® and Recurdyn®. The CDPR model used in the simulations is the one for the 3-cable under-constrained CDPR used in the experiments,

https://doi.org/10.1017/S0263574719000687 Published online by Cambridge University Press

Table I. Parameters associated with the under-constrained CDPR system used in the experiments.

Description	**Specification**
Workspace dimension	2 m × 2 m × 2 m
Payload radius	0.115 m
Payload mass	0.795 kg
Payload moment of inertia I_{xx}	3.104×10^{-3} kg·m^2
Payload moment of inertia I_{yy}	3.104×10^{-3} kg·m^2
Payload moment of inertia I_{zz}	6.204×10^{-3} kg·m^2

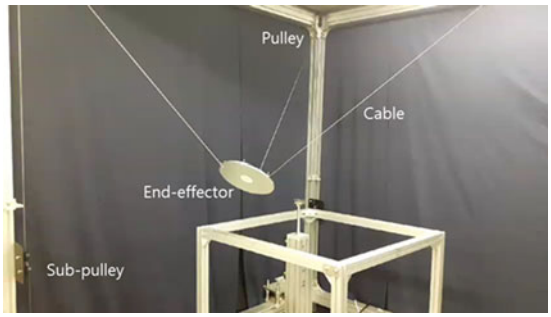


Fig. 5. The under-constrained CDPR system used in the experiment.

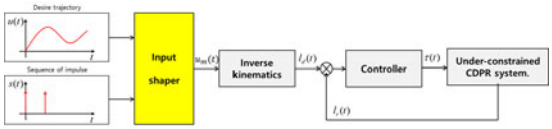


Fig. 6. A block diagram of the under-constrained CDPR control system used in the simulations and experiments.

which is shown in Fig. 5. Key parameters of the CDPR are listed in Table I, where the moment of inertia is for the end-effector *combined with* an inertial measurement unit (IMU) installed on it. In these simulations, the cables are assumed to be inextensible and massless.

The block diagram of the overall system used in the simulations as well as experiments is shown in Fig. 6. The original position command of the end-effector passes through a filter called the input shaper. Based on the filtered position command of the end-effector, the desired length of each cable is computed in the inverse kinematics. And a PID controller is used for each cable to make its actual length follow the desired one, and the same control gains used in the PID controller were used in all of the simulations.

4.1.1. Motion on horizontal plane.

Circular motion. In the first simulation, the focus was on how well the system would track a given circular path on a horizontal plane. The end-effector stayed at a single point on the circular path, point P, for 2 s (between $t = 0$ s and $t = 2$ s). And then it started moving and followed a given circular trajectory with a constant angular velocity in the next 5 s (between $t = 2$ s and $t = 7$ s). After completing a single circular motion, it stopped at point P and stayed there afterwards.

To verify the performance of the proposed method in reducing the sizes of transient and residual vibrations, the circular trajectories were used: one with a constant angular velocity, one with a trapezoidal angular velocity, one with input-shaping filter based on the circular trajectory with the constant angular velocity, and one with a continuous angular jerk. Figure 7 shows these four desired circular trajectories based on a circular path of 0.35 m in radius on the horizontal plane with a height of 1 m in z-direction. Their angular velocity and acceleration profiles are shown in Fig. 8, where the dotted, solid-blue, solid-red and solid-cyan lines are for a constant velocity profile, a trapezoidal

https://doi.org/10.1017/S0263574719000687 Published online by Cambridge University Press

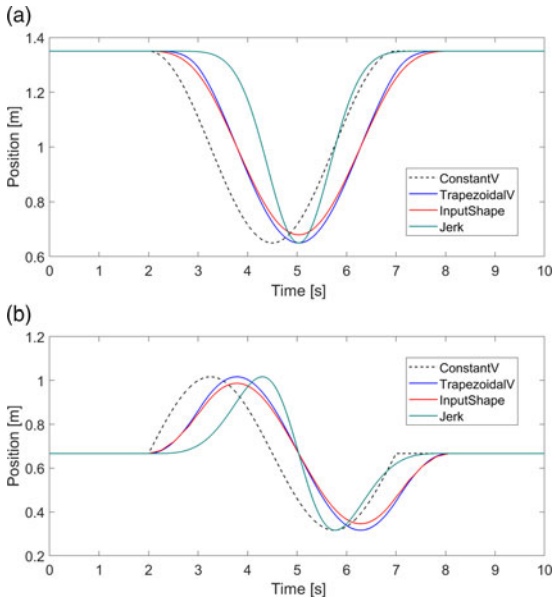


Fig. 7. A circular trajectory of the end-effector: (a) trajectory in x-direction and (b) trajectory in y-direction.

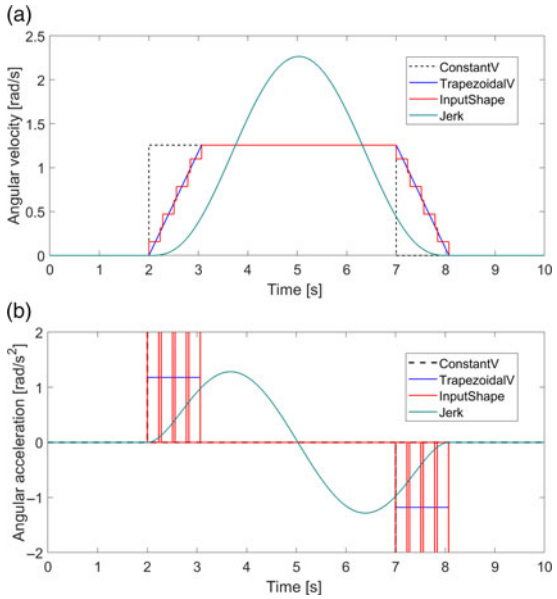


Fig. 8. Angular velocity and acceleration profiles for circular motions.

velocity profile, the input-shaped profile, and a continuous jerk, respectively. Note that an inevitable time delay exists in the input-shaped trajectory since the constant velocity trajectory is convoluted with impulses in the process of the input shaping.

The changes of the orientations, when the end-effect moves along the circular trajectory, are an inevitable consequence of the under-constrained CDPR system since the orientation of the end-effector changes as the end-effector position changes even in the equilibrium. The residual vibrations were persistent and did not decay, as shown in Fig. 9, since there is no damping elements in the simulation model.

Unwanted oscillations of the end-effector in the positions and orientations were subsided most when the input-shaping filter was used as shown in Fig. 9. The trajectory with the trapezoidal velocity profile showed good characteristics in suppressing the unwanted oscillations, even though it could not match the performance of the input-shaping filter. The RMS values measured for 8 s after completing a motion for the translational and orientational residual oscillations of the end-effector are

https://doi.org/10.1017/S0263574719000687 Published online by Cambridge University Press

Table II. The RMS of the translational and rotational residual oscillations in the simulations of a circular motion.

Oscillation type	**Constant**	**Trapezoidal**	**Input shape**	**Jerk**
Translational (mm)	20.76	7.80	3.96	29.19
Rotational (degree)	19.27	3.89	1.94	14.54

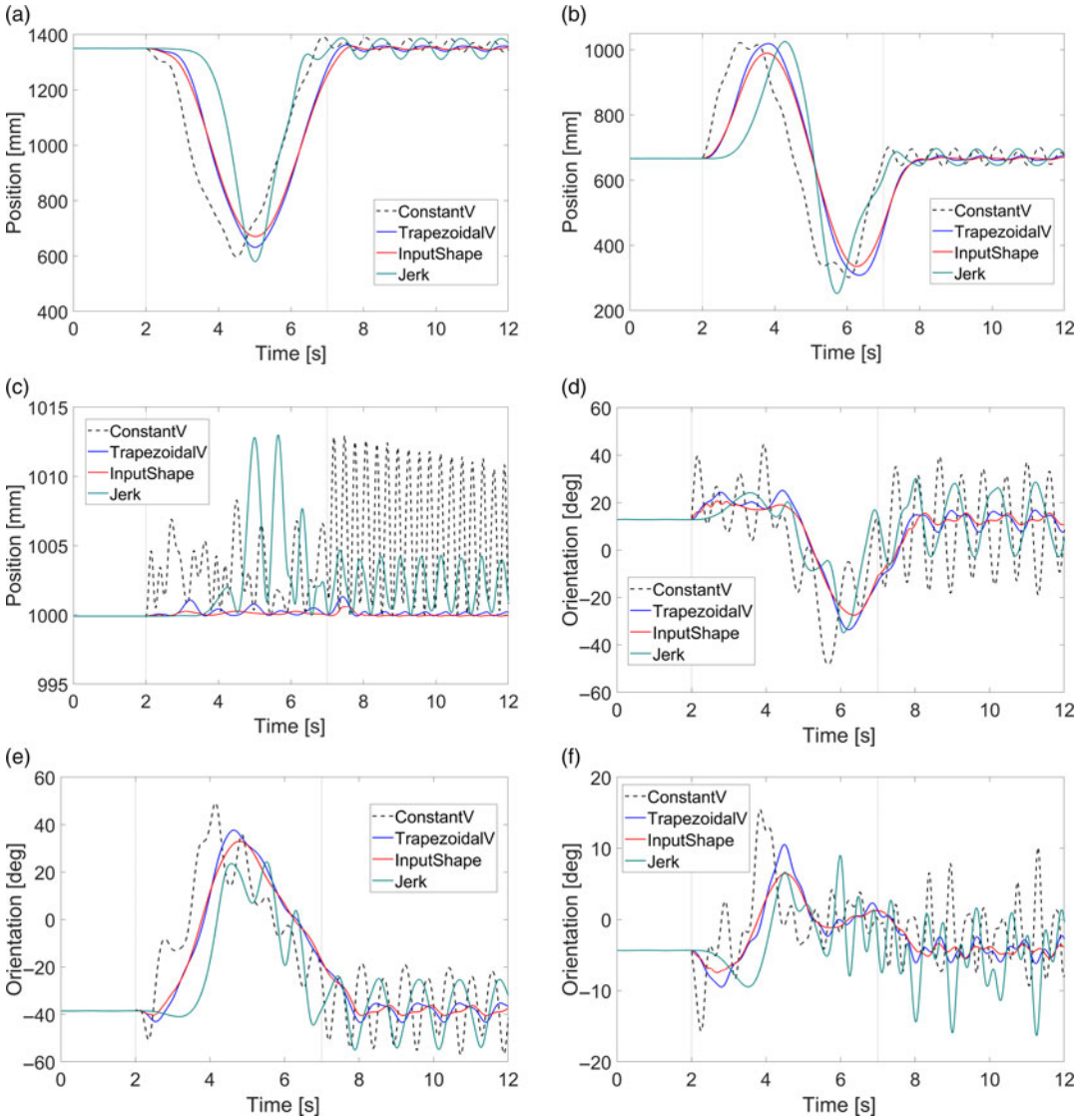


Fig. 9. Simulation results for a circular trajectory of 0.35 m in radius: (a) position in the x-direction; (b) position in the y-direction; (c) position in the z-direction; (d) roll angle; (e) pitch angle; and (f) yaw angle.

summarized in Table II. The former is defined as the square-root of the sum of the RMS values in the x-, y- and z-directional motions; and the latter is defined as the square-root of the sum of the RMS values in the roll, pitch and yaw motions.

https://doi.org/10.1017/S0263574719000687 Published online by Cambridge University Press

Table III. The RMS of the translational and rotational residual oscillations in the simulations of motion along a straight line.

Oscillation type	**Constant**	**Trapezoidal**	**Input shape**	**Jerk**
Translational (mm)	15.09	5.11	3.07	8.62
Rotational (degree)	16.37	4.67	2.26	6.34

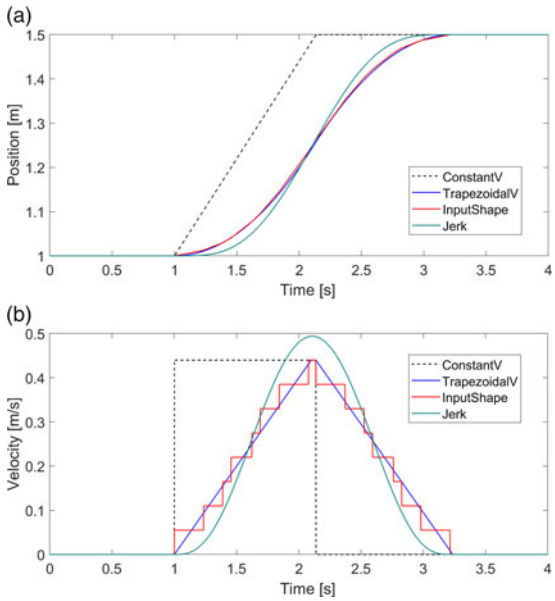


Fig. 10. Desired trajectories and velocity profiles for motions along a straight line.

Motion along straight line. For a motion along a straight line, the starting and the ending points are different and the system natural frequencies at these points are different. In order to see how this difference in the frequencies affects the transient and residual vibrations of the end-effector, additional simulations were performed. The end-effector started its motion in the x-direction from the rest at $x = 1.00$ m and then stopped after traveling 0.5 m, that is, at $x = 1.50$ m. Figure 10 shows the straight-line motion trajectories in position and velocity. The three natural frequencies change along the motion path as shown in Fig. 11. The one in blue in the plot ranges from 2.13 to 2.60 Hz, the orange from 1.29 to 2.11 Hz and the yellow from 0.89 to 1.10 Hz.

Despite the fact that the natural frequency at start of the motion is different from that at the final position of end-effector, the transitional and residual oscillations of the end-effector were suppressed when the input-shaped trajectory was generated by the proposed method, which can be observed in Fig. 12. The RMS values on the residual vibrations are listed in Table III and that were measured for 8 s after completing a motion.

4.1.2. Motion in 3-D space. To verify the effectiveness and performance of the proposed method when there is the difference of the natural frequencies between the start point and the end point of the path, motions based on spiral paths in z-direction were simulated additionally. All the conditions for the simulations are the same as the ones in Section 4.1.1 except the z-direction. The end-effector rises from 1.0 to 1.1, 1.3 and 1.5 m, and falls from 1.0 to 0.9, 0.7 and 0.5 m for the spiral motions. The natural frequencies of initial point and final point of the path are shown in Fig. 13. The oscillations of the end-effector in the orientations are shown in Fig. 14.

https://doi.org/10.1017/S0263574719000687 Published online by Cambridge University Press

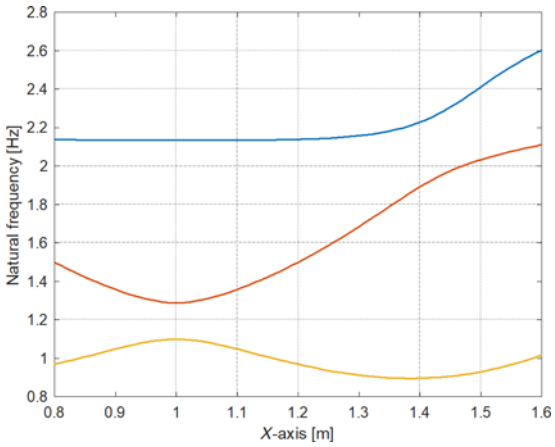


Fig. 11. The three natural frequencies change as the end-effector changes its position in the x-direction.

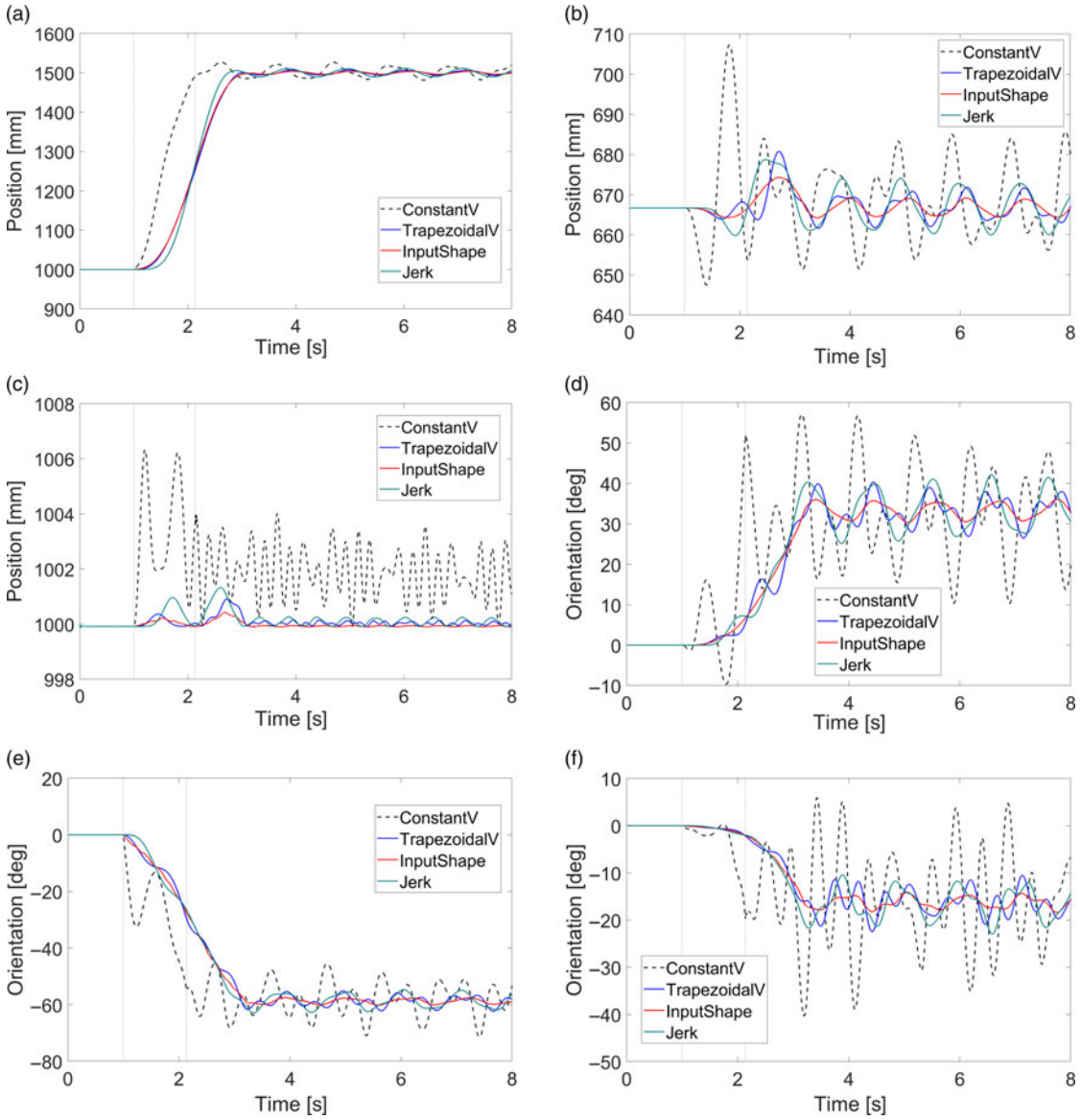


Fig. 12. Simulation results for a straight-line motion: (a) position in the x-direction; (b) position in the y-direction; (c) position in the z-direction; (d) roll angle; (e) pitch angle; and (f) yaw angle.

https://doi.org/10.1017/S0263574719000687 Published online by Cambridge University Press

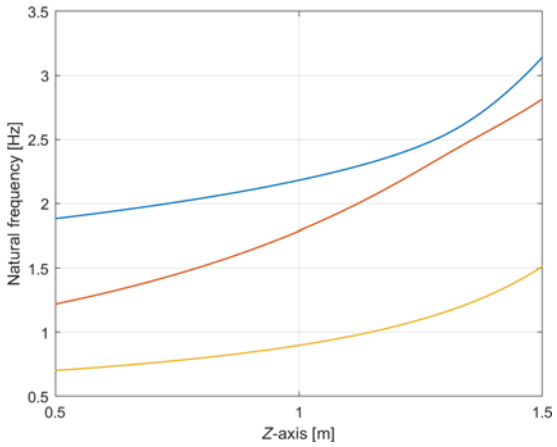


Fig. 13. The three natural frequencies change as the end-effector changes its position in the z-direction.

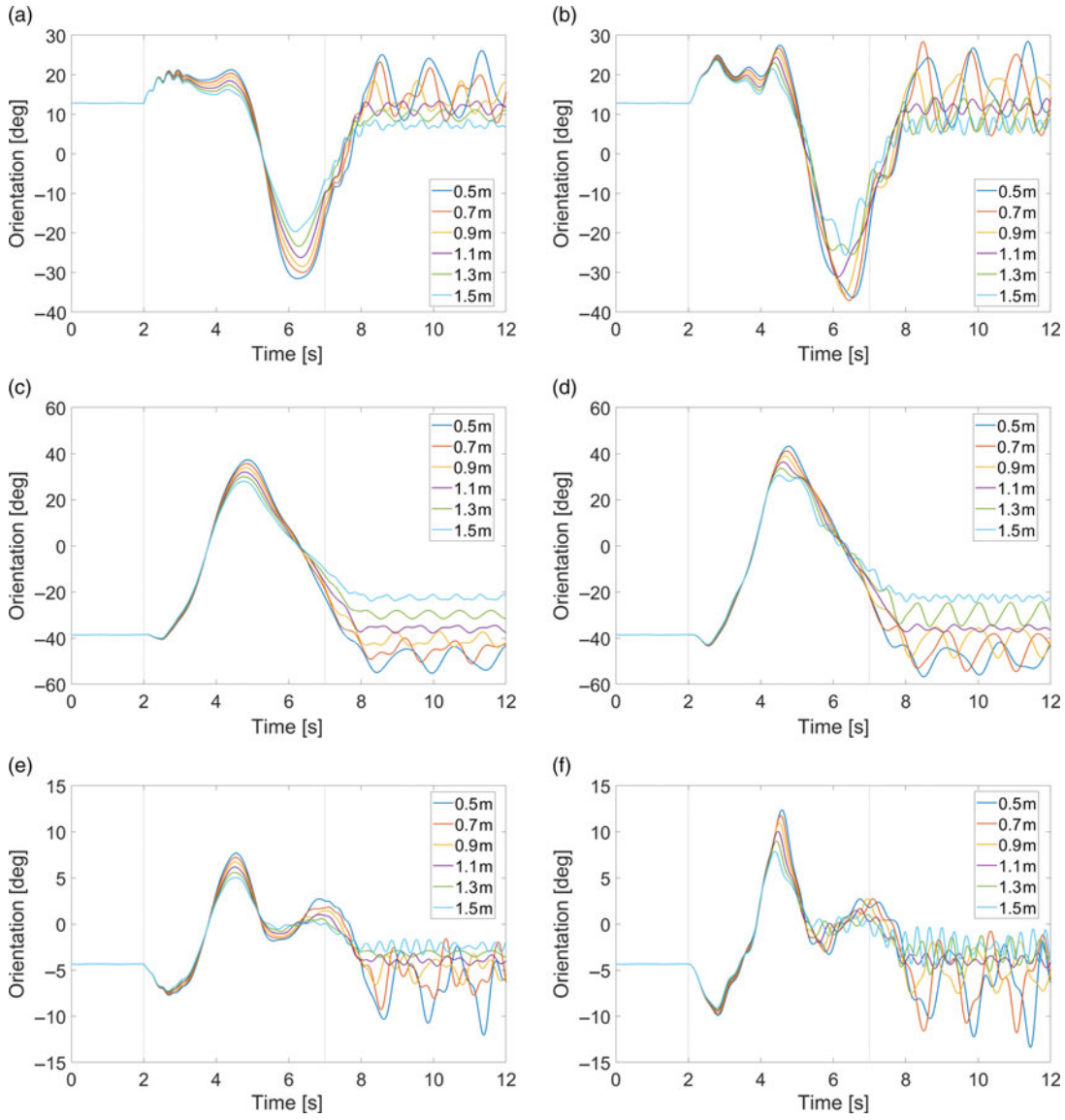


Fig. 14. Simulation results for a circular motion with input-shaped filter when the final point is not same as the initial point: (a) roll angle when input shaped trajectory is used; (b) roll angle when trajectory based on trapezoidal velocity profile is used; (c) pitch angle when input shaped trajectory is used; (d) pitch angle when trajectory based on trapezoidal velocity profile is used; (e) yaw angle when input shaped trajectory is used; and (f) yaw angle when trajectory based on trapezoidal velocity profile is used.

https://doi.org/10.1017/S0263574719000687 Published online by Cambridge University Press

Table IV. The RMS of the residual *rotational* oscillations in the experiments (unit: degrees).

Motion type	**Constant**	**Trapezoidal**	**Input shaped**	**Jerk**
Circular	11.22	2.42	1.31	9.36
Linear	6.85	1.71	1.06	5.29

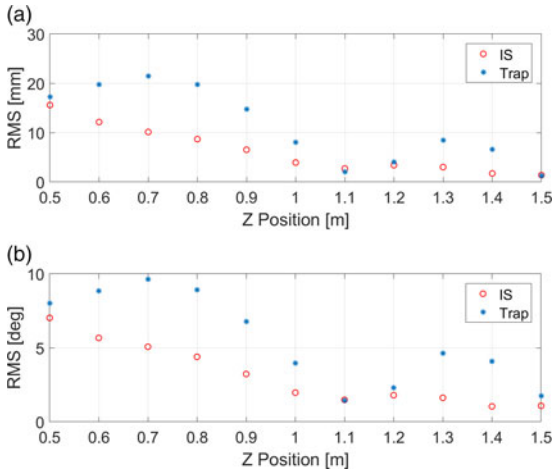


Fig. 15. RMS of rotational and rotational residual oscillations in the simulation of a circular motion: (a) RMS of translational residual oscillations and (b) RMS of rotational residual oscillations.

And the RMS values of the translational and rotational residual oscillations are shown in Fig. 15 when the input-shaped spiral trajectories and spiral trajectories with trapezoidal velocity profiles were applied and that were measured for 8 s after completing a spiral motion. The amplitude and the period of residual vibrations tend to be reduced when the position of the end-effector rises in z-direction, because the cable tension is increased. Despite the difference in the natural frequencies at the initial position and final positions of the trajectory, the performance of the trajectories with input shaping is better than that of the trajectories based on the trapezoidal velocity profiles.

4.2. Experiments

The cables used in the CDPR are made of stainless steel, and their diameter is 1.0 mm. Each of the three winches to drive, the cables are actuated by a pair of AC servomotors (Model: Beckhoff AM3024) and AC motor drives (Model: Beckhoff AX5203). Thus, the pose of the end-effector of the CDPR can be regulated by the servo system which directly controls the lengths of the three cables. Each of the three sub-pulleys was installed in the middle of a vertical post. Each of the three idling pulleys was installed at the top of its vertical post in order to make it possible to change the direction of the cable when the end-effector moves. An IMU sensor (Model: LORD MicroStrain® 3DM-GX5-45) was installed at the end-effector to measure the roll, pitch and yaw angle of the end-effector.

In the experiments, the four different trajectories used in the simulations were tried. The same circular path used in the simulations was used in the experiments. For the straight-line trajectory with a constant speed, it took 1.14 s to finish the motion.

The results in the experiments were similar to those in the simulations for both circular and straight-line motions on horizontal plane and spiral motions in *3D* space. As shown in Figs. 16 and 17, the unwanted vibrations were significantly suppressed when the input-shaped trajectory or trajectory with trapezoidal velocity was used. Among the two, the input-shaped trajectory was

https://doi.org/10.1017/S0263574719000687 Published online by Cambridge University Press

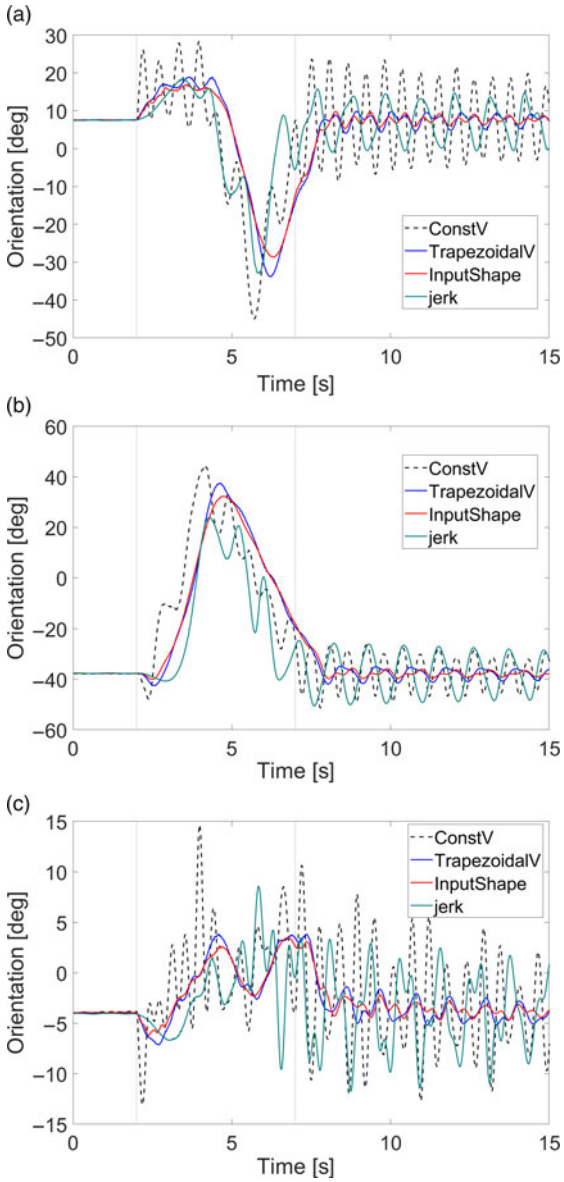


Fig. 16. Experimental data with roll, pitch and yaw angles of the end-effector based on a circular trajectory of 0.35 m in radius: (a) roll angle; (b) pitch angle; and (c) yaw angle.

better in suppressing unwanted oscillations. With the input-shaping method, the residual vibrations were reduced by 45.5% and 38.0%, respectively, for a circular and linear motions, compared with the trapezoidal velocity profile, which is summarized in Table IV. In cases of the spiral motions, the performance of the input-shaped trajectories is also better than that of the trajectories based on the trapezoidal velocity, and Fig. 18 shows the measured orientations of the end-effector.

By the way there is a difference between experimental and simulation results. The residual vibrations did not decay in the simulations as shown in Figs. 9, 12 and 14; however, they decreased slowly in the experiments, as shown in Figs. 16–18. This difference is caused by energy loss elements in the hardware which were neglected in the simulation model, such as pulley friction and damping/friction in the cables.

https://doi.org/10.1017/S0263574719000687 Published online by Cambridge University Press

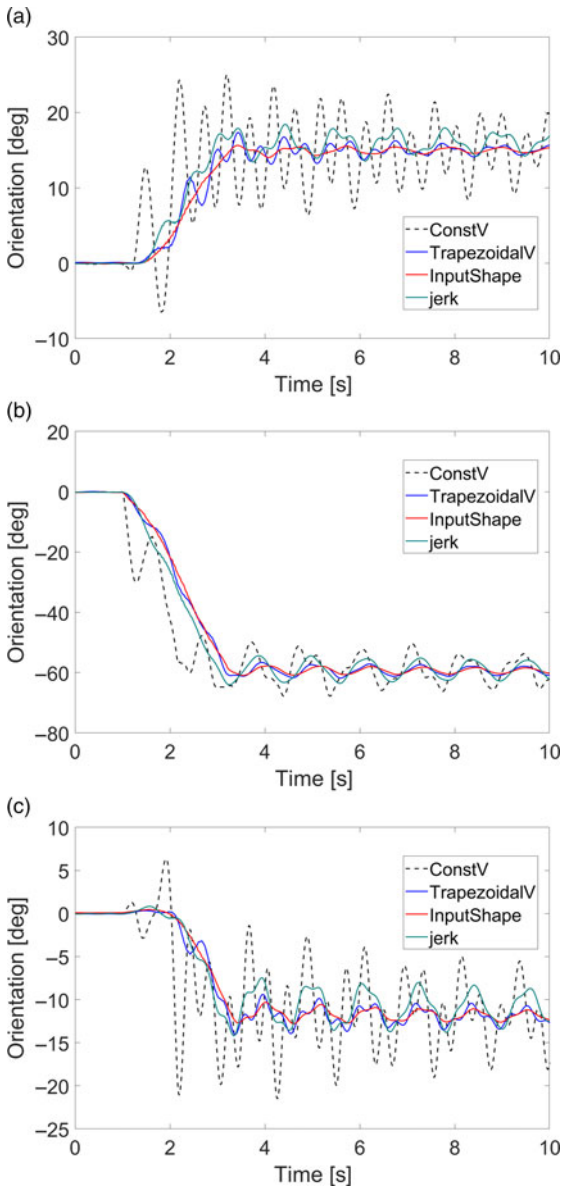


Fig. 17. Experimental data with roll, pitch and yaw angles of the end-effector based on a straight-line trajectory of 0.5 m in moving distance; (a) roll angle; (b) pitch angle; and (c) yaw angle.

5. Conclusion

In this paper, a trajectory generation method to suppress unwanted sway or vibrations related with under-constrained CDPR system was proposed, and simulations and experiments were conducted to verify the effectiveness and performance of the proposed method. The trajectory which reduces the unwanted oscillations is generated by applying multi-mode input shaping based on zero-vibration method. For this, the analysis of natural frequency of 3-cable under-constrained CDPR system was conducted by solving and linearizing the dynamics around an equilibrium point with the perturbation method. It is verified through simulations and experiments that unwanted oscillations in under-constrained CDPRs can be suppressed by using the proposed method.

https://doi.org/10.1017/S0263574719000687 Published online by Cambridge University Press

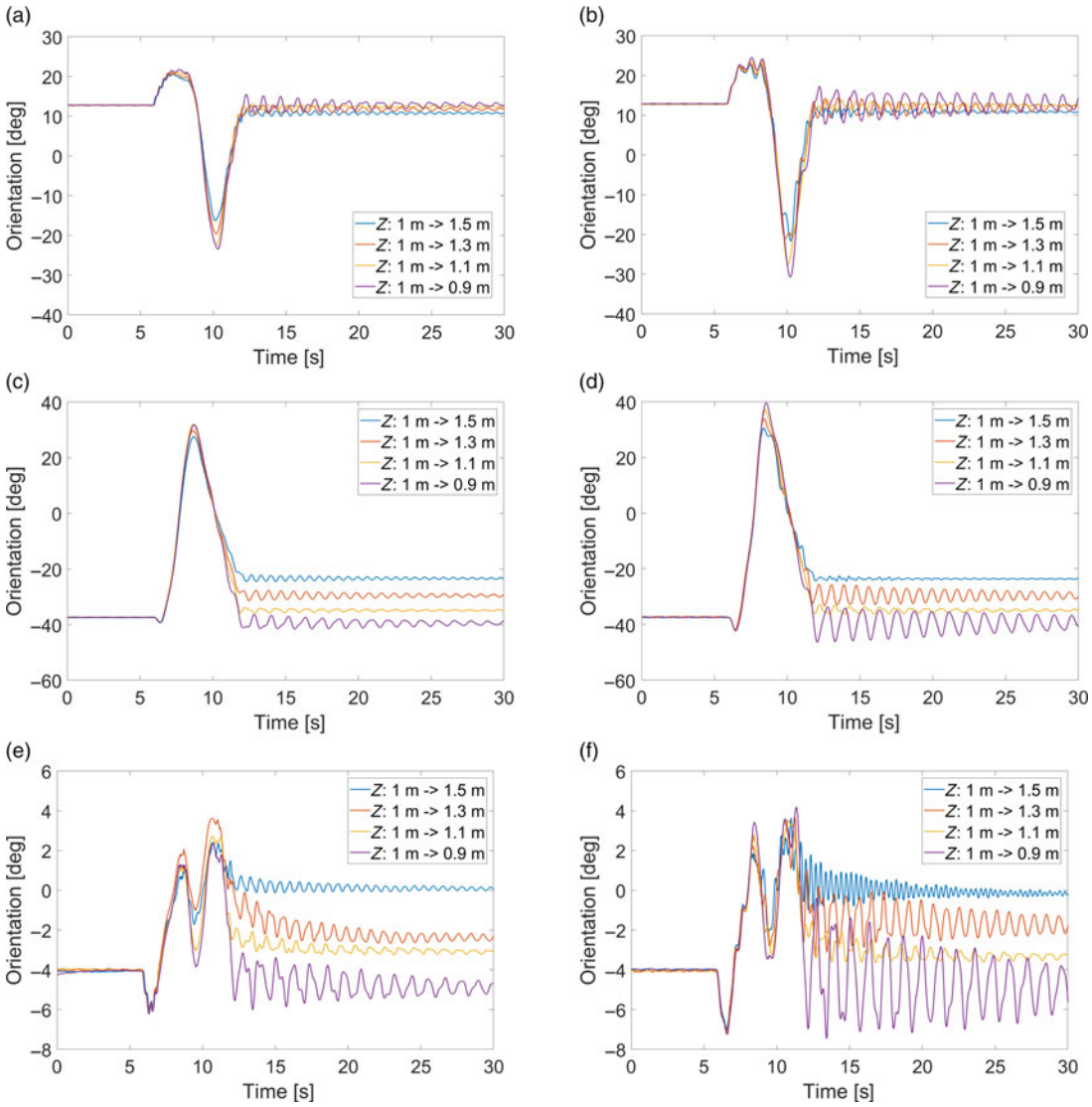


Fig. 18. Experimental data with roll, pitch and yaw angles of the end-effector based on a spiral trajectories: (a) roll angle when input shaped trajectory is used; (b) roll angle when trajectory based on trapezoidal velocity profile is used; (c) pitch angle when input shaped trajectory is used; (d) pitch angle when trajectory based on trapezoidal velocity profile is used; (e) yaw angle when input shaped trajectory is used; and (f) yaw angle when trajectory based on trapezoidal velocity profile is used.

Acknowledgment

This research was supported by Leading Foreign Research Institute Recruitment Program through the National Research Foundation of Korea (NRF) funded by the Ministry of Education, Science and Technology (MEST) (2012K1A4A3026740).

References

1. A. Pott, C. Meyer and A. Verl, "Large-Scale Assembly of Solar Power Plants with Parallel Cable Robots," *International Symposium on Robotics (ISR) and 6th German Conference on Robotics (ROBOTIK)*, Munich, Germany (2010) pp. 1–6.
2. R. Williams and L. Robert, "Five-hundred meter aperture spherical radio telescope (FAST) cable-suspended robot model and comparison with the arecibo observatory," Internet Publication (2015).
3. J. Albus, R. Bostelman and N. Dagalakis, "The NIST robocrane," *J. Field Robot.* **10**(5), 709–724 (1993).
4. R. G. Roberts, T. Graham and T. Lippitts, "On the inverse kinematics, statics, and fault tolerance of cable-suspended robots," *J. Field Robot.* **15**(10), 581–597 (1998).
5. S. Kawamura, H. Kino and C. Won, "High-speed manipulation by using parallel wire-driven robots," *Robotica* **18**(1), 13–21 (2000).

https://doi.org/10.1017/S0263574719000687 Published online by Cambridge University Press

6. S. Tadokoro, Y. Murao, M. Hiller, R. Murata, H. Kohkawa and T. Matsushima, "A motion base with 6-DOF by parallel cable drive architecture," *IEEE-ASME T. Mech.* **7**(2), 115–123 (2002).
7. M. Hiller, S. Fang, S. Mielczarek, R. Verhoeven and D. Franitza, "Design, analysis and realization of tendon-based parallel manipulators," *Mech. Mach. Theory* **40**(4), 429–445 (2005).
8. A. Alikhani, S. Behzadipour, S. A. S. Vanini and A. Alasty, "Workspace analysis of a three DOF cable-driven mechanism," *J. Mech. Robot.* **1**(4), 0410051–0410057 (2009).
9. D. Surdilovic, J. Zhang and R. Bernhardt, "STRING-MAN: Wire-Robot Technology for safe, flexible and Human-Friendly Gait Rehabilitation," *IEEE International Conference on Rehabilitation Robotics*, Noordwijk, Netherlands (2007) pp. 446–453.
10. G. Rosati, P. Gallina and S. Masiero, "Design, implementation and clinical tests of a wire-based robot for neurorehabilitation," *IEEE Trans. Neural. Syst. Rehabil. Eng.* **15**(4), 560–569 (2007).
11. J.-P. Merlet and D. Daney, "A Portable, Modular Parallel Wire Crane for Rescue Operations," *IEEE International Conference on Robotics and Automation*, Anchorage, AK, USA (2010) pp. 2834–2839.
12. M. Gobbi, G. Mastinu and G. Previati, "A method for measuring the inertia properties of rigid bodies," *Mech. Syst. Signal Process.* **25**(1), 305–318 (2011).
13. J. M. McCarthy, "21st century kinematics: synthesis, compliance, and tensegrity," *J. Mech. Robot.* **3**(2), 020201 (2011).
14. M. Carricato, "Direct geometrico-static problem of underconstrained cable-driven parallel robots with three cables," *J. Mech. Robot.* **5**(3), 031008 (2013).
15. M. Carricato and G. Abbasnejad, "Direct geometrico-static analysis of under-constrained cable-driven parallel robots with 4 cables," **In**: *Cable-Driven Parallel Robots* (T. Bruckmann and A. Pott, eds) (Springer, Berlin, Heidelberg, 2013) pp. 269–285.
16. M. Carricato and J.-P. Merlet, "Geometrico-static analysis of under-constrained cable-driven parallel robots," **In**: *Advances in Robot Kinematics: Motion in Man and Machine* (J. Lenarcic and M. M. Stanisic, eds) (Springer, Dordrecht, 2010) pp. 309–319.
17. G. Abbasnejad and M. Carricato, "Real solutions of the direct geometrico-static problem of under-constrained cable-driven parallel robots with 3 cables: A numerical investigation," *Meccanica* **47**(7), 1761–1773 (2012).
18. A. Berti, J.-P. Merlet and M. Carricato, "Solving the direct geometrico-static problem of 3-3 cable-driven parallel robots by interval analysis: Preliminary results," **In**: *Cable-Driven Parallel Robots* (T. Bruckmann and A. Pott, eds), (Springer, Berlin, Heidelberg, 2013) pp. 251–268.
19. G. Abbasnejad and M. Carricato, "Direct geometrico-static problem of underconstrained cable-driven parallel robots with *n* cables," *IEEE T. Robot.* **31**(2), 468–478 (2015).
20. M. Carricato, G. Abbasnejad and D. Walter, "Inverse geometrico-static analysis of under-constrained cable-driven parallel robots with four cables," **In**: *Latest Advances in Robot Kinematics* (J. Lenarcic and M. Husty, eds), (Springer, Dordrecht, 2012) pp. 365–372.
21. M. Carricato, "Inverse geometrico-static problem of underconstrained cable-driven parallel robots with three cables," *J. Mech. Robot.* **5**(3), 031002 (2013).
22. M. Carricato and J.-P. Merlet, "Stability analysis of underconstrained cable-driven parallel robots," *IEEE T. Robot.* **29**(1), 288–296 (2013).
23. A. Berti, J.-P. Merlet and M. Carricato, "Solving the direct geometrico-static problem of underconstrained cable-driven parallel robots by interval analysis," *Int. J. Rob. Res.* **35**(6), 723–739 (2016).
24. M. Zarei, A. Aflakian, A. Kalhor and M. T. Masouleh, "Oscillation damping of nonlinear control systems based on the phase trajectory length concept: An experimental case study on a cable-driven parallel robot," *Mech. Mach. Theory* **126**, 377–396 (2018).
25. N. Yanai, M. Yamamoto and A. Mohri, "Inverse Dynamics Analysis and Trajectory Generation of Incompletely Restrained Wire-Suspended Mechanisms," *IEEE International Conference on Robotics and Automation*, vol. 4, Seoul, South Korea (2001) pp. 3489–3494.
26. M. Yamamoto, N. Yanai and A. Mohri, "Trajectory control of incompletely restrained parallel-wire-suspended mechanism based on inverse dynamics," *IEEE T. Robot.* **20**(5), 840–850 (2004).
27. T. Heyden and C. Woernle, "Dynamics and flatness-based control of a kinematically undetermined cable suspension manipulator," *Multibody Syst. Dyn.* **16**(2), 155 (2006).
28. M. Yamamoto, N. Yanai and A. Mohri, "Inverse Dynamics and Control of Crane-Type Manipulator," *IEEE/RSJ International Conference on Intelligent Robots and Systems*, vol. 2, Kyongju, South Korea (1999) pp. 1228–1233.
29. C. Gosselin, P. Ren and S. Foucault, "Dynamic Trajectory Planning of a Two-DOF Cable-Suspended Parallel Robot," *IEEE International Conference on Robotics and Automation*, Saint Paul, MN, USA (2012) pp. 1476–1481.
30. C. Gosselin, "Global planning of dynamically feasible trajectories for three-DOF spatial cable-suspended parallel robots," **In**: *Cable-Driven Parallel Robots* (T. Bruckmann and A. Pott, eds), (Springer, Berlin, Heidelberg, 2013) pp. 3–22.
31. C. Gosselin and S. Foucault, "Dynamic point-to-point trajectory planning of a two-DOF cable-suspended parallel robot," *IEEE T. Robot.* **30**(3), 728–736 (2014).
32. N. Zhang and W. Shang, "Dynamic trajectory planning of a 3-DOF under-constrained cable-driven parallel robot," *Mech. Mach. Theory* **98**, 21–35 (2016).
33. J. Park, O. Kwon and J. H. Park, "Anti-sway trajectory generation of incompletely restrained wire-suspended system," *J. Mech. Sci. Technol.* **27**(10), 3171–3176 (2013).

https://doi.org/10.1017/S0263574719000687 Published online by Cambridge University Press

34. L. Ramli, Z. Mohamed and H. Jaafar, "A neural network-based input shaping for swing suppression of an overhead crane under payload hoisting and mass variations," *Mech. Syst. Signal Process.* **107**, 484–501 (2018).
35. E. Idá, A. Berti, T. Bruckmann and M. Carricato, "Rest-to-rest trajectory planning for planar underactuated cable-driven parallel robots," **In**: *Cable-Driven Parallel Robots* (C. Gosselin, P. Cardou, T. Bruckmann and A. Pott, eds), (Springer, Cham, 2018) pp. 207–218.
36. S. W. Hwang, J.-H. Bak, J. Yoon, J. H. Park and J.-O. Park, "Trajectory generation to suppress oscillations in under-constrained cable-driven parallel robots," *J. Mech. Sci. Technol.* **30**(12), 5689–5697 (2016).
37. C.-T. Chen, *Linear System Theory and Design* (Oxford University Press, New York, NY, 1998).
38. T. D. Tuttle and W. P. Seering, "A Zero-Placement Technique for Designing Shaped Inputs to Suppress Multiple-Mode Vibration," *Proceedings of American Control Conference*, Baltimore, MD, USA (1994) pp. 2533–2537.
39. L. Y. Pao, "Multi-input shaping design for vibration reduction," *Automatica* **35**(1), 81–89 (1999).
40. T. Singh and W. Singhose, "Input shaping/time delay control of maneuvering flexible structures," *Proceedings of the 2002 American Control Conference*, Anchorage, AK, USA (2002) pp. 1717–1731.

Appendix A

A. Perturbations

Kinematic constraints are satisfied even at equilibrium points, that is, when $\mathbf{x}(t) = \mathbf{x}_0$ and $\boldsymbol{\eta}(t) = \boldsymbol{\eta}_0$:

$$\phi_i(\mathbf{x}_0, \boldsymbol{\eta}_0) = 0, \quad i = 1, 2, 3. \tag{A1}$$

Since these constraints must be valid any time, even with perturbations,

$$\phi_i(\mathbf{x}_0 + \delta\mathbf{x}, \boldsymbol{\eta}_0 + \delta\boldsymbol{\eta}) = 0, \quad i = 1, 2, 3. \tag{A2}$$

Using the Taylor series expansion, Eq. (A2) becomes

$$\phi_i(\mathbf{x}_0, \boldsymbol{\eta}_0) + \left.\frac{\partial \phi_i}{\partial \mathbf{x}}\right|_0 \delta\mathbf{x} + \left.\frac{\partial \phi_i}{\partial \boldsymbol{\eta}}\right|_0 \delta\boldsymbol{\eta} + \text{h.o.t} = 0, \quad i = 1, 2, 3. \tag{A3}$$

Using Eq. (A1), Eq. (A3) becomes, up to first-degree of perturbation variables,

$$\left.\frac{\partial \phi_i}{\partial \mathbf{x}}\right|_0 \delta\mathbf{x} + \left.\frac{\partial \phi_i}{\partial \boldsymbol{\eta}}\right|_0 \delta\boldsymbol{\eta} = 0, \quad i = 1, 2, 3. \tag{A4}$$

Differentiating the constraints with respect to time, that is,

$$\frac{d}{dt}\phi_i(\mathbf{x}, \boldsymbol{\eta}) = \mathbf{0}, \quad i = 1, 2, 3 \tag{A5}$$

yields

$$\frac{\partial \phi_i}{\partial \mathbf{x}}\dot{\mathbf{x}} + \frac{\partial \phi_i}{\partial \boldsymbol{\eta}}\dot{\boldsymbol{\eta}} = \mathbf{0}. \quad i = 1, 2, 3. \tag{A6}$$

With perturbations at the equilibrium point, $\dot{\mathbf{x}} = \dot{\mathbf{x}}_0 + \delta\dot{\mathbf{x}}$ and $\dot{\boldsymbol{\eta}} = \dot{\boldsymbol{\eta}}_0 + \delta\dot{\boldsymbol{\eta}}$ with $\dot{\mathbf{x}}_0 = \dot{\boldsymbol{\eta}}_0 = \mathbf{0}$

$$\left.\frac{\partial \phi_i}{\partial \mathbf{x}}\right|_0 \delta\dot{\mathbf{x}} + \left.\frac{\partial \phi_i}{\partial \boldsymbol{\eta}}\right|_0 \delta\dot{\boldsymbol{\eta}} = \mathbf{0}, \quad i = 1, 2, 3. \tag{A7}$$

Differentiating Eq. (A6) with respect to time, that is,

$$\frac{d}{dt}\left(\frac{\partial \phi_i}{\partial \mathbf{x}}\dot{\mathbf{x}} + \frac{\partial \phi_i}{\partial \boldsymbol{\eta}}\dot{\boldsymbol{\eta}}\right) = \mathbf{0}, \quad i = 1, 2, 3 \tag{A8}$$

yields

$$\frac{d}{dt}\left(\frac{\partial \phi_i}{\partial \mathbf{x}}\right)\dot{\mathbf{x}} + \frac{\partial \phi_i}{\partial \mathbf{x}}\ddot{\mathbf{x}} + \frac{d}{dt}\left(\frac{\partial \phi_i}{\partial \boldsymbol{\eta}}\right)\dot{\boldsymbol{\eta}} + \frac{\partial \phi_i}{\partial \boldsymbol{\eta}}\ddot{\boldsymbol{\eta}} = \mathbf{0}, \quad i = 1, 2, 3. \tag{A9}$$

https://doi.org/10.1017/S0263574719000687 Published online by Cambridge University Press

$$\left(\frac{\partial^2 \phi_i}{\partial \mathbf{x}^2}\dot{\mathbf{x}} + \frac{\partial^2 \phi_i}{\partial \boldsymbol{\eta}\,\partial \mathbf{x}}\dot{\boldsymbol{\eta}}\right)\dot{\mathbf{x}} + \left(\frac{\partial^2 \phi_i}{\partial \boldsymbol{\eta}^2}\dot{\boldsymbol{\eta}} + \frac{\partial^2 \phi_i}{\partial \mathbf{x}\,\partial \boldsymbol{\eta}}\dot{\mathbf{x}}\right)\dot{\boldsymbol{\eta}} + \frac{\partial \phi_i}{\partial \mathbf{x}}\ddot{\mathbf{x}} + \frac{\partial \phi_i}{\partial \boldsymbol{\eta}}\ddot{\boldsymbol{\eta}} = \mathbf{0}, \quad i = 1, 2, 3. \tag{A10}$$

With perturbations at the equilibrium point, $\dot{\mathbf{x}} = \dot{\mathbf{x}}_0 + \delta\dot{\mathbf{x}}$, $\ddot{\mathbf{x}} = \ddot{\mathbf{x}}_0 + \delta\ddot{\mathbf{x}}$, $\dot{\boldsymbol{\eta}} = \dot{\boldsymbol{\eta}}_0 + \delta\dot{\boldsymbol{\eta}}$ and $\ddot{\boldsymbol{\eta}} = \ddot{\boldsymbol{\eta}}_0 + \delta\ddot{\boldsymbol{\eta}}$ with $\dot{\mathbf{x}}_0 = \dot{\boldsymbol{\eta}}_0 = \ddot{\mathbf{x}}_0 = \ddot{\boldsymbol{\eta}}_0 = \mathbf{0}$, Eq. (A10) can be rewritten up to the first degree of perturbation variables as

$$\left.\frac{\partial \phi_i}{\partial \mathbf{x}}\right|_0 \delta\ddot{\mathbf{x}} + \left.\frac{\partial \phi_i}{\partial \boldsymbol{\eta}}\right|_0 \delta\ddot{\boldsymbol{\eta}} = \mathbf{0}, \quad i = 1, 2, 3. \tag{A11}$$

Using vector notation, Eqs. (A4), (A7) and (A11) can be written as Eqs. (21), (22) and (23), respectively.

https://doi.org/10.1017/S0263574719000687 Published online by Cambridge University Press